International Journal of Concrete Structures and Materials

RESEARCH Open Access

Simplified Constitutive and Damage Plasticity Models for UHPFRC with Different Types of Fiber

Doaa Talib Hashim[1], Farzad Hejazi[1*] and Voo Yen Lei[2]

Abstract

In this study, several simplified constitutive models and a damage plasticity model for ultra-high performance fiber reinforced concrete(UHPFRC)material with micro and hooked ends steel fibers, Bekaert Dramix 5D steel fiber, and Forta-Ferro synthetic fiber had been developed. Later, these constitutive and damage plasticity models were applied as analytical model to numerically simulate the concrete members with different fibers, and to evaluate the behavior of the concrete sections. The constitutive models for UHPFRC of three mix designs were obtained experimentally by conducting uniaxial compression and tensile tests on both cylinder and dog-bone specimens. Next, a comparison was made among the three mix designs based on the outcomes retrieved from uniaxial compression and tensile stress–strain. These results were validated by numerically analyzing three hollow circular columns via finite element method. The numerical results revealed that the proposed material model possessed appropriate tensile strain-hardening behavior and uniaxial compression strengths of UHPFRC with different types of fiber. The lateral resistance responses of the tested hollow sections, which were obtained by using developed constitutive and damage plasticity models, displayed exceptional agreement with the experimental outcomes.

Keywords: UHPFRC, constitutive model, uniaxial tensile testing techniques, uniaxial compressive testing techniques, stress–strain curve, different types of fiber

1 Introduction

Ultra-high performance concrete (UHPC) refers to an innovative concrete that is defined based on multiple criteria (Naaman and Wille 2012; Rossi 2008). Ultra-high performance fiber reinforced concrete (UHPFRC) exhibits its superior mechanical properties and energy absorption capacity mainly due to its slow water to binder ratio, high binder dosage, and relatively high fiber dosage (Yu et al. 2015).

The compressive strength of UHPC material is mostly above 150 MPa. A range of fiber materials have been implemented in UHPFRC to achieve the specified requirements for structural concrete (ACI Committee, 239).The resulting hardened concrete can yield compressive strength as much as 200 MPa, ascribed to its homogenous and dense microstructure (Graybeal 2006; Yunsheng et al. 2008). Nevertheless, concrete is brittle in nature, despite its high compressive strength.

Having that said, the need for durability, ductility, and workability has led to the development of UHPC and UHPFRC (El-Dieb 2009; Hassan et al. 2012; Rossi 2013). Fiber has the most critical role in determining the ductility behavior of UHPFRC structure until flexural failure. Due to the presence of fiber in UHPFRC, the ultimate tensile strain capacity of up to 5×10^{-3} can be achieved (Rossi et al. 2005).

Wuest et al. (2008) proposed a meso-mechanical based model to predict the tensile response of UHPFRC by

*Correspondence: farzad@fhejazi.com
[1] Department of Civil Engineering Faculty, University Putra Malaysia, Serdang, Selangor 43400, Malaysia
Full list of author information is available at the end of the article
Journal information: ISSN 1976-0485 / eISSN 2234-1315

taking into account several parameters, such as aspect-ratio, volume, orientation, distribution of fibers, and mechanical properties of the matrix.

At present, UHPFRC is in demand for civil engineering applications due to its exceptional post-cracking ductility behavior under flexure and tension, particularly when bending prevails (Richard and Cheyrezy 1995). Nonetheless, this essential feature is affected by the fiber properties used, including strength, stiffness, volume fraction, geometry, Poisson's ratio, interface properties, shape, and fiber distribution (Kim et al. 2008; Yoo et al. 2013).

Fiber length or aspect ratio has been proven to be one of the most convincing approaches to improve strength, fracture energy, and flexural performance of UHPFRC. It increases the effective bond area between matrix and fiber at crack interfacial zones (Aydın and Baradan 2013; Yoo et al. 2013; Lankard 1972). However, some of the challenges involved are fiber balling and poor fiber distribution, especially upon increasing fiber aspect ratio and length (Lankard 1972; Li 2012). Ferrara et al. (2011) assessed the tensile performance of UHPFRC, and found that the performance was highly affected by fiber orientation and distribution. As a result, it was suggested the casting process should be carried out carefully to ascertain fiber enhancement.

In another study, Farzad et al. (2019) found that the effect of low macro cell currents calculated for UHPC samples, when compared to NSC samples, was clearly visible in the calculation results. It was revealed that repaired UHPC consumed more time to damage after repair than conventional concrete did, thus suggesting that service life could be protracted. According to Ng et al. (2016), it is highly imperative to have an insight into the fiber behavior in tension. They added that the steel fibers had crack paths in concrete to find their way through sections with poor fiber dispersion and/or divert around the fiber ends (Ng et al. 2016).

Synthetic fibers are artificially fabricated fibers that can be categorized into three groups based on the materials used for fabrication process, namely micro-synthetic, macro-synthetic, and polypropylene fibers. Macro-synthetic fibers are usually incorporated into concrete to control cracks in concrete slabs. They display outstanding performance and are effective in ground subjected to high deformation. These fibers are excellent when used as corrosion resistance material. Their low density and post-crack performance makes them eco-friendly and cost effective in terms of logistics requirement in remote areas. In comparison to steel fibers, macro-synthetic fibers show very little time-dependent extension over cracks when subject to flexural action. These fibers vary in behavior depending on fiber scheme and load.

The constitutive law for concrete material is usually derived by using uniaxial, biaxial, and triaxial tests. However, constitutive law is mostly used in uniaxial compression tests, while the plastic evolution at early age under triaxial stress state is always neglected (Bofang 2013). Mahmud et al. (2013) recommended parameters that define the concrete material by conducting experimental tests.

The literature depicts that many types of steel and synthetic fiber are used to reinforce UHPFRC. Hence, recent studies have highlighted that due to the availability of vast fiber materials, the effect of these different types of fiber, including steel and synthetic fibers, on the strength of structural members in UHPFRC material demands detailed investigation. This is mainly due to the lack of suitable and reliable experimental testing data.

In this present study, three types of fiber were used to mix micro and hooked ends steel fibers, 5D steel fibers, and Forta-Ferro synthetic fibers. Next, in order to simulate the UHPFRC material using finite element method, simplified constitutive and damage plasticity models for UHPFRC material with micro and hooked ends steel fibers, Bekaert Dramix 5D steel fiber, and Forta-Ferro synthetic fiber were developed. For this purpose, both uniaxial compression and tensile tests were performed on cylinder and dog-bone specimens that had been casted using the selected fibers. Next, a comparison was made among the three mix designs based on the results retrieved from uniaxial tensile and compressive stress–strain tests. After that, the constitutive and damage plasticity models were implemented in finite element program as analytical model parameters for the considered concrete materials, in order to conduct numerical analysis by modeling the UHPFRC hollow columns with different types of fibers and comparing the outcomes with the experimental findings. The experimental tests were conducted to evaluate the behavior of hollow thin circular columns with varied types of fiber and to verify the results of finite element analysis.

2 Development of Constitutive Model

In this study, experimental tests were conducted on UHPFRC specimens of micro and hooked ends steel fibers, Bekaert Dramix 5D steel fibers, and Forta-Ferro synthetic fibers to develop a constitutive model for UHPFRC, as well as to propose material damage plasticity parameters. Uniaxial tensile and compressive tests were conducted on dog-bone and cylinder control specimens, respectively, in order to propose the damage plasticity parameters and to develop constitutive models for the three mix designs. A constitutive model for the UHPFRC

material was developed based on the experiment test of concrete samples in compression and tension, as illustrated in Fig. 1.

3 Materials and Mix Design

The UHPFRC refers to a concrete mixture composed of mainly fine aggregates and homogenous cementations composite, which is capable of attaining compressive strength exceeding 150 MPa. The material composition of UHPFRC matrix includes Portland cement Type I, tap water, and silica fume. The mix proportion adhered to that prescribed by Wille et al. (2014). This study used three types of fiber, namely micro and hooked ends steel fiber, 5D steel fibers, and Forta-Ferro synthetic fibers. A constitutive material model for the aforementioned materials is required to develop a reliable and effective damage plasticity model. Thus, an experiment was conducted to incorporate the results into the finite element simulation as concrete material properties. Three mix designs were prepared using different types of fiber. In this present study, the reference concrete mixture (T1) refers to the first mix design for UHPFRC reinforced with cooper-coated micro and hooked-ends steel fibers. It is a blend of very high strength micro-steel fibers, hooked-ends steel fibers, and cementitious binders with extremely low water content. Based on ASTM A820, EN 14889, and YB/T151-1998; cooper-coated micro steel fiber (WSF0220) has tensile strength above 2300 MPa at 0.2 ± 0.05 mm diameter and 20 ± 1 mm length (see Fig. 2a). Meanwhile, cooper-coated

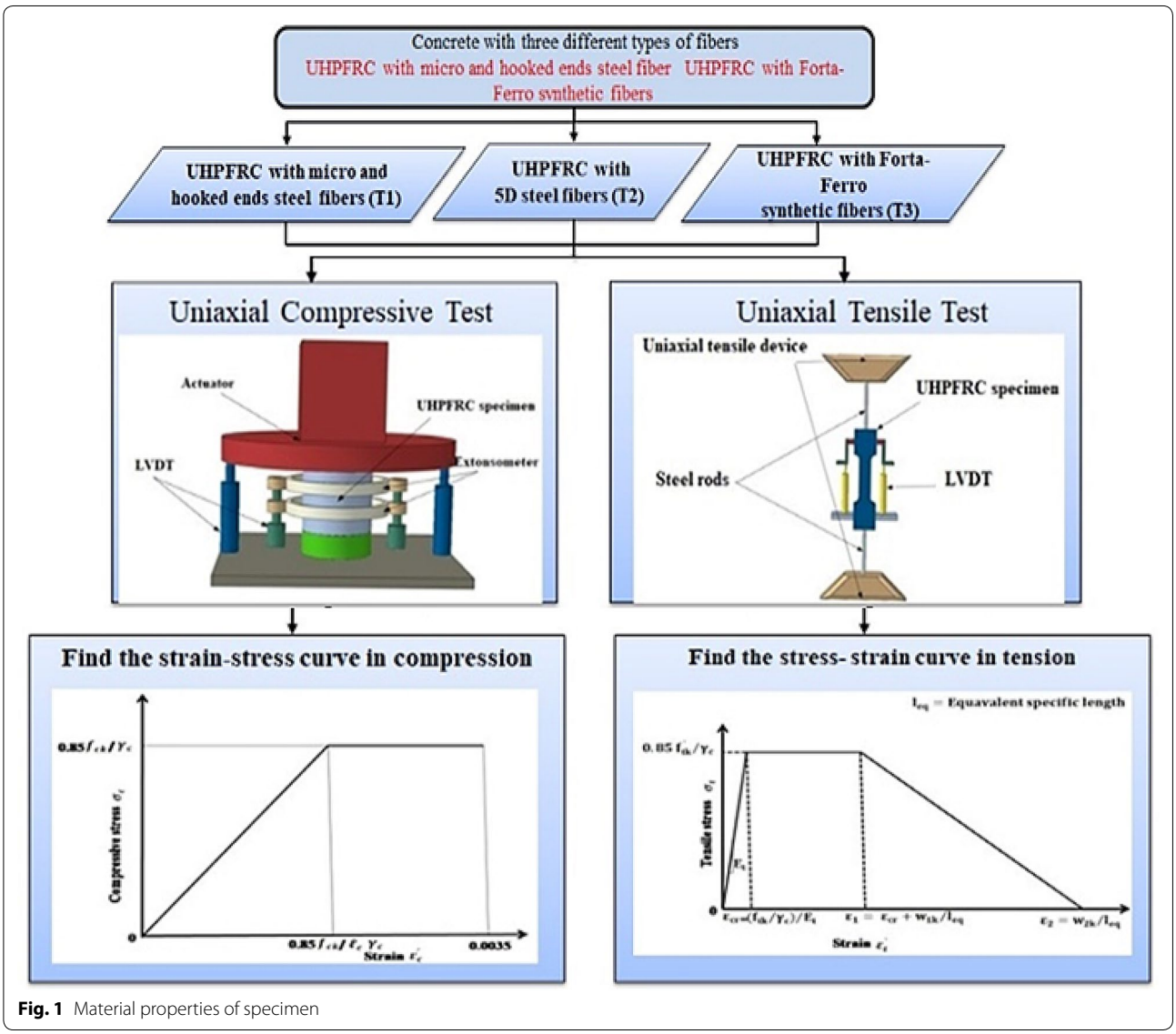

Fig. 1 Material properties of specimen

hooked-ends steel fiber (C-GSF0325) has tensile strength exceeding 2500 MPa at 0.3 ± 0.05 mm diameter and 25 ± 1 mm length (see Fig. 2b). Fig. 2c displays the 5D steel fibers used for the second mix design (T2). It has tensile strength above 2.3 MPa with 0.9 mm diameter and 60 mm length. Lastly, the Forta-Ferro synthetic fiber (see Fig. 2d) was used in the third UHPFRC mix design (T3),which consisted of Virgin polypropylene and copolymer with 570–660 MPa tensile strength at 54 mm length. Table 1 tabulates the mix design components for T1, T2, and T3.

4 Specimen Preparation and Experimental Setup

Three UHPFRC mix designs were mixed in this experimental work, namely: UHPFRC with cooper-coated micro and hooked-ends steel fibers, UHPFRC reinforced with 5D steel fibers, and UHPFRC reinforced with Forta-Ferro synthetic fibers. Table 2 presents the specimen details for the constitutive model test experiment.

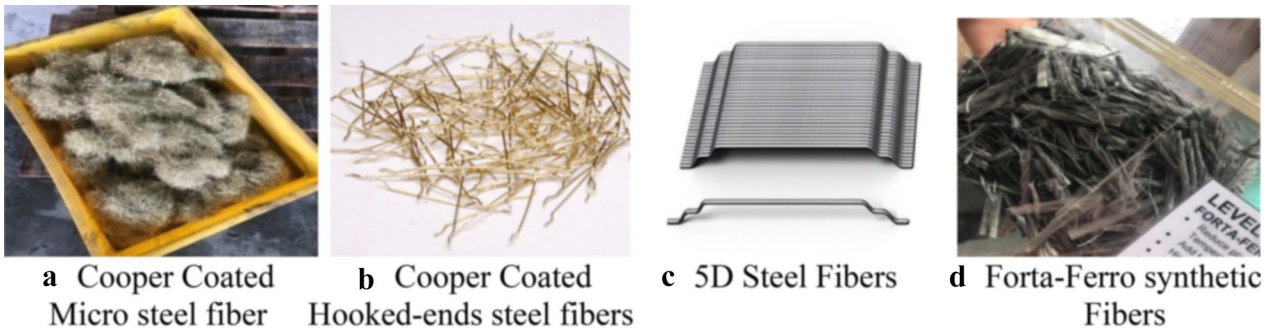

Fig. 2 The considered different types of fibers

Table 1 Mix designs for UHPFRC with different fiber types

Material	UHPFRC with cooper coated micro and hooked-ends steel fibers (T1) (kg/m^3)	UHPFRC with 5D steel fibers (T2) (kg/m^3)	UHPFRC with Forta-Ferro synthetic fibers (T3) (kg/m^3)
Cement	850	850	850
Densified silica fume (SF90)	200	200	200
Dry silica fine sand 30/100 PB	695	695	695
Dry silica coarse sand 16/30 PB	295	295	295
Silica VC2644	40	40	40
Fiber	158	60	1
Free water	140	140	140
3% moisture	30.93	30.93	30.93
Total air voids	–	–	–
Total	2408.93	2310.93	2251.93

Table 2 Uniaxial tensile and compressive tests specimens

No.	Specimen type	Mix design	Age (days)		
18	Dog-bone	UHPFRC with micro and hooked ends steel fibers	7	14	28
18	Dog-bone	UHPFRC with 5D steel fibers	7	14	28
18	Dog-bone	UHPFRC with Forta-Ferro synthetic fibers	7	14	28
9	Cylinder	UHPFRC with micro and hooked ends steel fibers	7	14	28
9	Cylinder	UHPFRC with 5D steel fibers	7	14	28
9	Cylinder	UHPFRC with Forta-Ferro synthetic fibers	7	14	28

4.1 Direct Tensile Test

The exact method that can capture the real tensile strength of UHPFRC and UHPC is the uniaxial tensile test. Despite the challenges posed in performing this test, one test method employed in this study was to use dog-bone specimens. The specimens were casted in a dog-bone form so that a uniaxial stress field could be generated through the central section of the specimen, wherein localization of cracks and failure typically occur in this area.

Two geometries of un-notched dog-bone specimens at 200 mm length were prepared. The cross-section of the specimens was 50×50 mm at the ends and a prismatic middle portion at 26×50 mm with 25 or 50 mm of each end of the specimens (see Fig. 3). The tapered section was equal to two fiber lengths (13 mm) in order to avoid fiber balling. This ensured that the fibers were randomly distributed to avoid premature failure. The length of the notched cross-section was 126 and 76 mm, respectively. All the specimens were used to develop a new constitutive model for UHPFRC using three types of fiber. Additionally, this experiment was conducted to facilitate the evaluation of UHPFRC damage plasticity. The UHPFRC mechanical, chemical, and physical properties of the materials are reported by (Yang et al. 2009).

The test was carried out by preparing jig and steel handles to connect the 12 mm diameter steel reinforcement bars to the specimen. The specimen was held in position with the aid of jigs supported from both ends of the specimen to prevent misalignment. The two handles were attached to the specimen at each end and were used as the grip for the testing machine. The test was setup on a SHIMADZU displacement control machine of capacity 50 kN, as illustrated in Fig. 4. An electronic camera was fixed in front of the specimen for displacement measurement of the narrow cross section. The displacement control used in this experiment was applied to the steel rods at 0.4 mm/min rate. The tensile load transmitted on to the specimen was recorded. A load–displacement curve was generated and the equivalent stress–strain curve was developed for both ascending and descending parts.

Fig. 4 Uniaxial tensile test setu

4.2 Compression Test

This study adhered to BS1881-121 and ASTMC469-94 in order to determine both compressive stress–strain values and modulus of elasticity for UHPFRC. The test methods defined in both standards, nonetheless, appeared inappropriate, particularly to measure the post-cracking behavior of UHPFRC specimens. Detailed discussion regarding the difficulties faced when performing both tests is presented in later sections of this paper. Therefore, with adjustments made to the standard tests, a simple method is proposed to attain the stress–strain range.

A total of 27 control concrete cylinder specimens with 75 mm diameter and 150 mm height were prepared (see Fig. 5). The cylindrical specimens were subjected to test

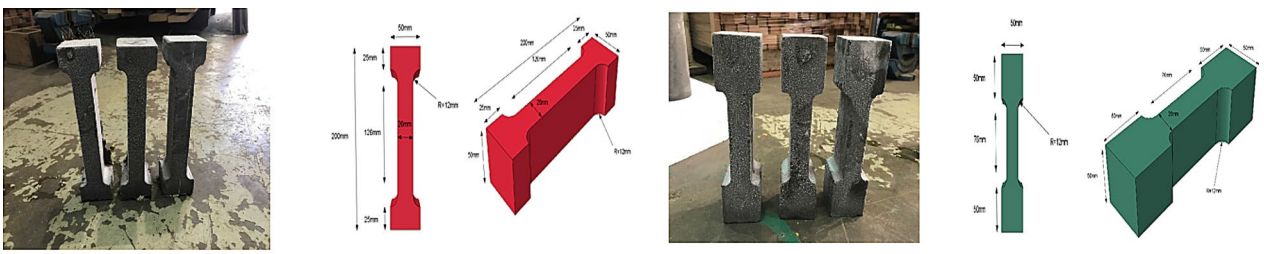

a Type I b Type II

Fig. 3 The dog-bone specimen geometries

Fig. 5 The cylinder specimens

Fig. 6 Test set up

at 7, 14, and 28 curing days. The same approach was adopted for all specimens to minimize the difference in behavior during testing. In particular, similar equipment and procedures were used for the casting and testing operations in all specimens. Full stress–strain curves were extracted for compression.

A uniaxial compression test was conducted on cylinder specimens (size: 75×150 mm), which is similar to that undertaken by Hassan et al. (2012). The method used two rigid circular rings secured at two-third height of the specimen using clamping screws in accordance to ASTM C469. One LVDT was employed to measure the displacement located in the rings on the opposite side of the specimen, as portrayed in Fig. 6. The elastic stage was determined from the displacement measured with the LVDT on the circular rings. The crosshead movement of the test machine was measured using another LVDT placed parallel to the specimen, because the crosshead of the machine had been fixed. Hence, an LVDT was placed parallel to the specimen to measure the crosshead movement of the test machine (see Fig. 6). The full compressive stress–strain response was extracted by combining results from the two sets. The fixed crosshead was used to avoid end constraint due to the friction between loading platen and specimen (Lu and Hsu 2006).

All cylinder specimens were grinded in line with the requirement of BS EN 12390-3:2009 prior to testing, in order to minimize uneven surfaces at each end. The tests were conducted using deflection control testing machine at 0.000667 mm/s rate and the results were recorded.

5 Constitutive Model and Damage Plasticity of UHPFRC with Different Types of Fiber

In this study, isotropic damaged elasticity after tensile and compressive tests were used to develop a concrete damage plasticity model. This model mimics the behavior of the concrete in a non-elastic manner. The total strain tensor, ε, is comprised of elastic part ε^{el}. and plastic part ε^{pl}, as expressed in Eqs. (1–4).

$$\boldsymbol{\varepsilon} = \boldsymbol{\varepsilon}^{\boldsymbol{el}} + \boldsymbol{\varepsilon}^{\boldsymbol{pl}} 0. \tag{1}$$

$$\boldsymbol{\sigma} = \boldsymbol{D}^{\boldsymbol{el}} : (\boldsymbol{\varepsilon} - \boldsymbol{\varepsilon}^{\boldsymbol{pl}}). \tag{2}$$

$$\bar{\boldsymbol{\sigma}} = \boldsymbol{D}_{\circ}^{\boldsymbol{el}} : (\boldsymbol{\varepsilon} - \boldsymbol{\varepsilon}^{\boldsymbol{pl}}). \tag{3}$$

$$\boldsymbol{D}^{\boldsymbol{el}} = (\mathbf{1} - \boldsymbol{d})\boldsymbol{D}_{\circ}^{\boldsymbol{el}} \tag{4}$$

The nominal stress with degraded elastic tensor in Eq. (4) is rewritten as Eq. (5):

$$\boldsymbol{\sigma} = (\mathbf{1} - \boldsymbol{d})\boldsymbol{D}_{\circ}^{\boldsymbol{el}} : (\boldsymbol{\varepsilon} - \boldsymbol{\varepsilon}^{\boldsymbol{pl}}). \tag{5}$$

The damage plasticity constitutive model was based on the following stress–rain relationship:

$$\boldsymbol{\sigma} = (1 - d) ==> \bar{\boldsymbol{\sigma}}\boldsymbol{\sigma} = (1 - \boldsymbol{d_t})\bar{\boldsymbol{\sigma}}_{\boldsymbol{t}} + (1 - \boldsymbol{d_c})\bar{\boldsymbol{\sigma}}_{\boldsymbol{c}} \tag{6}$$

(here d_t and d_c denote two scalar damage parameters that ranged a 0–1 to represent 'undamaged' and 'fully damaged', respectively (Grassl et al. 2013). The concrete damage was based on concrete damage plasticity model and considered the failure of tensile a compressive cracking and crushing, respectively. The isotropic hardening variables were expressed by inelastic compression and cracking strains, $\varepsilon_c^{\text{in},h}$ and $\varepsilon_t^{ck,h}$, respectively, which include the

plastic hardening strain, $\varepsilon^{pl,h}$, and the residual strain due to damages, as displayed in Eq. 7).

$$\dot{\boldsymbol{\varepsilon}}^{\boldsymbol{pl,h}} = \begin{bmatrix} \boldsymbol{\varepsilon}_{\boldsymbol{t}}^{\boldsymbol{pl,h}} \\ \boldsymbol{\varepsilon}_{\boldsymbol{c}}^{\boldsymbol{pl,h}} \end{bmatrix}; \boldsymbol{\varepsilon}^{\boldsymbol{pl}} = \boldsymbol{h}\,(\boldsymbol{\varepsilon}^{\boldsymbol{pl,h}},\ \bar{\boldsymbol{\sigma}})\dot{\boldsymbol{\varepsilon}}^{\boldsymbol{pl}}, \dot{\boldsymbol{\varepsilon}} = \dot{\boldsymbol{\varepsilon}}^{\boldsymbol{el}} + \dot{\boldsymbol{\varepsilon}}^{\boldsymbol{pl}} \tag{7}$$

The failure or yield surface is controlled by the hardening related to tension and compression behavior. The behavior of the concrete is described based on the assumption of yield function, f ($\varepsilon^{pl,h}$, $\bar{\sigma}$), which represents the yield surface in effective stress space that determines the state of failure or damage [35]. Thus, the flow rule is defined by the concrete damage plasticity model, as expressed in Eq. (8):

$$\dot{\boldsymbol{\varepsilon}}^{\boldsymbol{pl}} = \dot{\boldsymbol{\lambda}} \cdot \frac{\partial \boldsymbol{G}(\bar{\boldsymbol{\sigma}})}{\partial(\bar{\boldsymbol{\sigma}})} \tag{8}$$

The flow rule depicted above is not linked with the concrete damage plasticity model, thus indicating that the yield function of f ($\varepsilon^{pl,h}$, $\bar{\sigma}$) and the plastic potential of g_P did not coincide. Therefore, plastic potential was determined based on effective stress while the direction of the plastic flow, $\frac{\partial G(\bar{\sigma})}{\partial \bar{\sigma}}$, was not normal to the yield surface. Figure 7 presents the uniaxial tensile and compressive responses of the concrete influenced by the damaged plasticity behavior. This assumption was applied in the concrete damage plasticity model to develop compression and tension load, as expressed in Eqs. (9, 10).

$$\boldsymbol{\sigma}_{\boldsymbol{t}} = (\mathbf{1} - \boldsymbol{d}_{\boldsymbol{t}})\boldsymbol{E}_{\circ}(\boldsymbol{\varepsilon}_{\boldsymbol{t}} - \boldsymbol{\varepsilon}_{\boldsymbol{t}}^{\boldsymbol{pl,h}}) \tag{9}$$

$$\boldsymbol{\sigma}_{\boldsymbol{c}} = (\mathbf{1} - \boldsymbol{d}_{\boldsymbol{c}})\boldsymbol{E}_{\circ}(\boldsymbol{\varepsilon}_{\boldsymbol{c}} - \boldsymbol{\varepsilon}_{\boldsymbol{c}}^{\boldsymbol{pl,h}}) \tag{10}$$

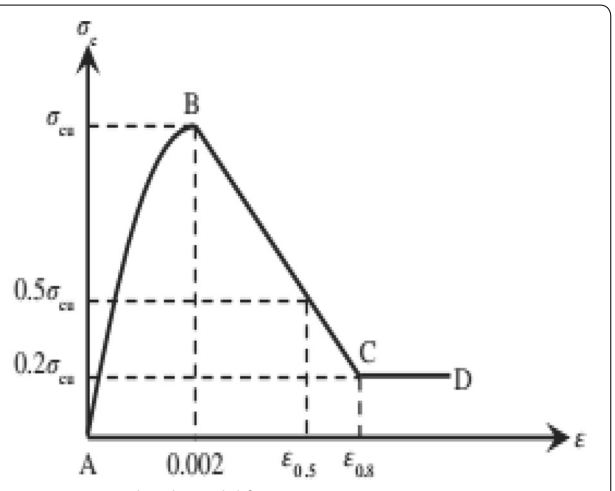

Fig. 7 Kent and Park model for

The effective uniaxial stresses, σ_t and σ_c, were derived as Eqs. 11 and 12, respectively:

$$\bar{\boldsymbol{\sigma}}_{\boldsymbol{t}} = \frac{\boldsymbol{\sigma}_{\boldsymbol{t}}}{(1 - \boldsymbol{d}_{\boldsymbol{t}})} = \boldsymbol{E}_{\circ}(\boldsymbol{\varepsilon}_{\boldsymbol{t}} - \boldsymbol{\varepsilon}_{\boldsymbol{t}}^{\boldsymbol{pl,h}}). \tag{11}$$

$$\bar{\boldsymbol{\sigma}}_{\boldsymbol{c}} = \frac{\boldsymbol{\sigma}_{\boldsymbol{c}}}{(1 - \boldsymbol{\sigma}_{\boldsymbol{c}})} = \boldsymbol{E}_{\circ}(\boldsymbol{\varepsilon}_{\boldsymbol{c}} - \boldsymbol{\varepsilon}_{\boldsymbol{c}}^{\boldsymbol{pl,h}}). \tag{12}$$

where, compressive strain is $\varepsilon_c = \varepsilon_c^{pl,h} + \varepsilon_c^{el}$, while tensile strain is $\varepsilon_t = \varepsilon_t^{pl,h} + \varepsilon_t^{el}$.

Hardening and softening variables were used to determine the crack and crush trends, respectively. These trends are responsible for the development and loss of yield surface and elastic stiffness, respectively. The damage behavior in compression and tension was characterized independently by the two hardening variables. These variables are represented by equivalent plastic strain in tension $\boldsymbol{\varepsilon}_{\boldsymbol{c}}^{\boldsymbol{pl,h}}$ and compression $\boldsymbol{\varepsilon}_{\boldsymbol{t}}^{\boldsymbol{pl,h}}$.

5.1 Compressive Behavior

Plastic hardening strain in compression $\varepsilon_c^{pl,h}$ plays a vital role in determining the correlation between damage parameters and compressive strength of concrete in nete damage plasticity models, as expressed in Eqs. (13–15) (see Fig. 7a).

$$\bar{\boldsymbol{\sigma}}_{\boldsymbol{c}} = \frac{\boldsymbol{\sigma}_{\boldsymbol{c}}}{(1 - \boldsymbol{\sigma}_{\boldsymbol{c}})} = \boldsymbol{E}_{\circ}(\varepsilon_c - \varepsilon_c^{(pl,h)}) \tag{13}$$

$$\begin{cases} \boldsymbol{\varepsilon}_{\boldsymbol{c}}^{\boldsymbol{in.h}} = \boldsymbol{\varepsilon}_{\boldsymbol{c}} - \frac{\boldsymbol{\sigma}_{\boldsymbol{c}}}{\boldsymbol{E}_{\circ}} \\ \boldsymbol{\varepsilon}_{\boldsymbol{c}}^{\boldsymbol{pl,h}} = \boldsymbol{\varepsilon}_{\boldsymbol{c}} - \frac{\boldsymbol{\sigma}_{\boldsymbol{c}}}{\boldsymbol{E}_{\circ}}\left(\frac{1}{1-\boldsymbol{d}_{\boldsymbol{c}}}\right) \end{cases} \tag{14}$$

$$\boldsymbol{\varepsilon}_{\boldsymbol{c}}^{\boldsymbol{pl,h}} = \boldsymbol{\varepsilon}_{\boldsymbol{c}}^{(in,h)} - \frac{\boldsymbol{d}_{\boldsymbol{c}}}{(1 - \boldsymbol{d}_{\boldsymbol{c}})}\frac{\boldsymbol{\sigma}_{\boldsymbol{c}}}{\boldsymbol{E}_{\circ}} \tag{15}$$

Typically, uniaxial compressive behavior is determined via experimental tests or constitutive models, as proposed by Hognestad (1951) and Kent and Park (Kent and Park 1971), for unconfined concrete. Figure 8 displayed a parabolic ascending part of curve (A), which signify the hardening stage, while a linear behavior descending part (B–C) for the softening stage of the confined and unconfined concrete behavior.

The softening part of the curve for unconfined cylinder continued until 20% of the compressive strength (Point C) to indicate that the stress value was restricted from further decrease. In this case, a perfect plastic behavior can be assumed following the softening trend (C–D) on the curve. The model is assumed parabolic to be less ambiguous.

It is critical, however, to define the concrete behavior up to 40% level of its strength in the elastic phase to

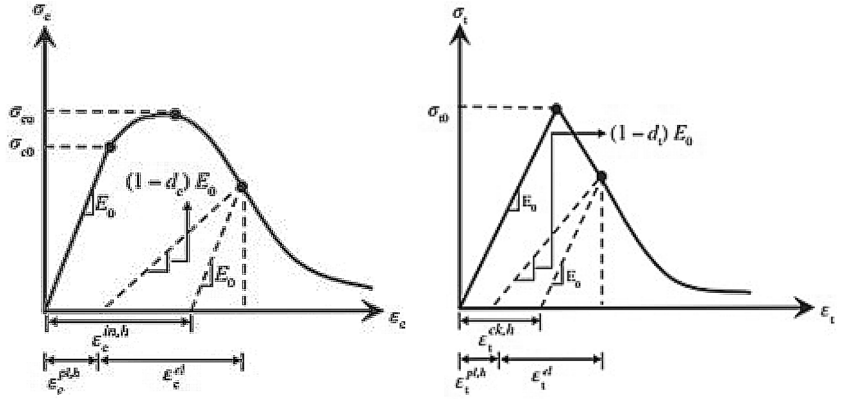

Fig. 8 Behavior of concrete to uniaxial loading stat (Hognestad 1951) confined and unconfined concrete (Kent and Park 1971)

attain elastic modulus. Figures 7a and 8 display the inelastic hardening strain in compression $\varepsilon_c^{in,h}$, as given in Eq. (16):

$$\boldsymbol{\varepsilon_c^{in,h} = \varepsilon_c - \frac{\sigma_c}{E_\circ}} \tag{16}$$

The cyclic behavior is defined by effective parameters that contribute to the concrete behavior, including damages in compression and tension. Compression damage ($\boldsymbol{d_c}$) was established based on inelastic hardening strain in compression, $\boldsymbol{\varepsilon_c^{in,h}}$, which controlled the unloading curve of the slope. Parameter d_c is expressed as Eq. (17), which increased with increase in $\boldsymbol{\varepsilon_c^{in,h}}$.

$$\boldsymbol{d_c = 1 - \frac{\sigma_c}{\sigma_{cu}}} \tag{17}$$

The tangent to the curve declined with respect to the modulus of elasticity, $E_\circ$, as the plastic strains increased due to the damage in brittle materials(see Fig. 7a). The damage parameter (d_c) at the maximum compressive stress was considered zero (0), and reduced to 0.8 at 20% of the remaining strength.

5.2 Uniaxial Tensile Behavior

The plastic hardening strain in tension $\varepsilon_t^{pl,h}$ portrayed in Fig. 7b is given in Eqs. (18–20):

$$\sigma_t = \frac{\sigma_t}{(1-\sigma_t)} = E_\circ(\varepsilon_t - \varepsilon_t^{pl,h}) \tag{18}$$

$$\begin{cases} \varepsilon_t^{ck.h} = \varepsilon_t - \frac{\sigma_t}{E_\circ} \\ \varepsilon_t^{pl,h} = \varepsilon_t - \frac{\sigma_t}{E_\circ}\left(\frac{1}{1-d_t}\right) \end{cases} \tag{19}$$

$$\varepsilon_t^{pl,h} = \varepsilon_t^{ck,h} - \frac{d_t}{(1-d_t)}\frac{\sigma_t}{E_\circ} \tag{20}$$

Figure 7b shows that increment in hardening cracking strain, $\varepsilon_t^{ck,h}$ increased the tension damage, as expressed in Eq. (21):

$$\boldsymbol{d_t = 1\frac{\sigma_t}{\sigma_{t^\circ}}} \tag{21}$$

6 Results and Discussion

Uniaxial tensile and compressive tests were conducted on dog-bone and cylinder specimens, respectively, to develop a constitutive model for UHPFRC using selected fibers and to propose a set of damage plasticity parameters.

6.1 Uniaxial Compression Test

For each mix design, the compression strength test was conducted on three cylinder specimens (size: 75 × 150 mm) for 7, 14, and 28 curing days, and the average result for each test was calculated. The results of stress versus strain curves are recorded for each test at 7, 14, and 28 curing days.

The strain values achieved for the elastic stage were obtained by taking the average displacement of LVDT positioned in circular rings divided by gauge length. The strain values were estimated by taking the average deformation of the LVDT obtained from the crosshead movement divided by the total height of the specimen. Next, the stress was determined from the ratio of the machine load to the cross-sectional area of the cylinder sample. The test method adhered to ASTMC469 (2002) with the aid of circular rings and LVDT positioned strategically around the test cylinder. The setup was designed in such

a way that the platen restricted in position to avoid movement together with the test machine. The total displacement of the crosshead refers to the total displacement of the sample and the area affected by the restrained platen at both ends. The platen turned this approach into an ambiguous method that might yield inconsistent results to cause higher or smaller strain values to be recorded for initial elastic modulus. This necessitated the use of both methods in order to minimize such issues. As such, the latest method was used, wherein the results were corrected until the initial elastic modulus and strain values are equal to the former method and were in the elastic region. Next, the results from both approaches were combined to form the stress–strain responses of the material. The amended crosshead readings were used to generate pre- and post-cracking behaviors of the system. The results displayed similar trend up to the first crack in both cases. Figure 9 illustrates the compressive stress–strain curves for the specimen with micro and hooked ends steel fiber, 5D steel fiber, and Forta-Ferro synthetic fiber concretes at varied specimen age. The particles in specimens for UHPFRC with micro and hooked ends steel fibers (T1) were very integrated due to the interaction between steel fibers and matrix that gave the samples more stability until its first crack.

The testing results showed that the surface of the concrete remained un-deformed, even at the stage of losing total strength (see Fig. 10). Figure 11a displays the strength development at different ages and the effect of fiber type on optimum compressive strength for UHPFRC with micro and hooked ends steel fibers (T1). The behavior of UHPFRC specimens seemed elastic up to 90–95% of the compressive strength, and this was followed by strain hardening up to the peak strength. Nevertheless, this behavior was not observed for all specimens. The outcomes signify a ductile failure, while the concrete surfaces remained plain despite total strength loss. Figure 9b presents the compressive stress–strain curves for UHPFRC with 5D steel fiber concrete at different ages. The elastic behavior of UHPFRC specimens (T2) had been up to 70–75% of their compressive values, and the strain hardening behavior was followed by compression hardening up to its optimum strength. The ductile compressive failure of T2 was due to the interaction between fibers and matrix, which contributed to ductile behavior of the material.

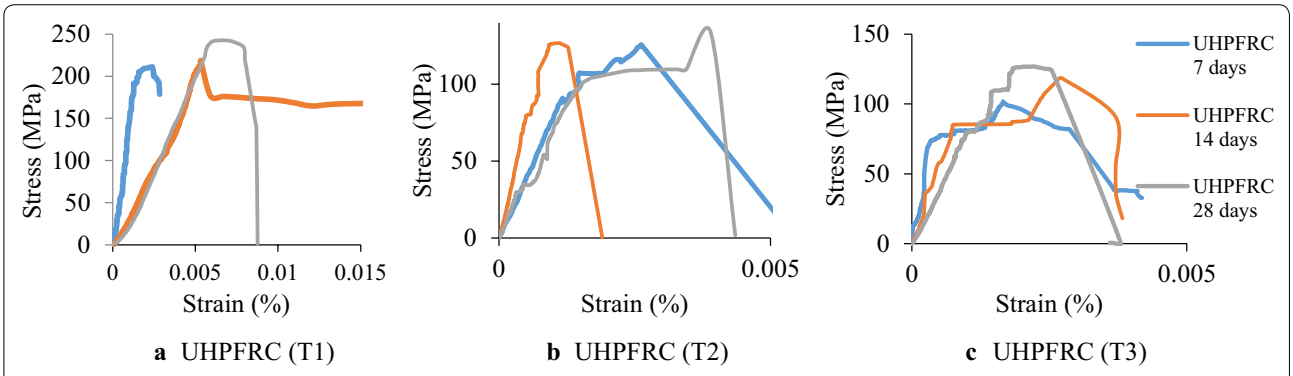

Fig. 9 Compressive stress–strain curve with respect to age

Fig. 10 Compression tests: formation of cracks and UHPFRC (T1) at failure

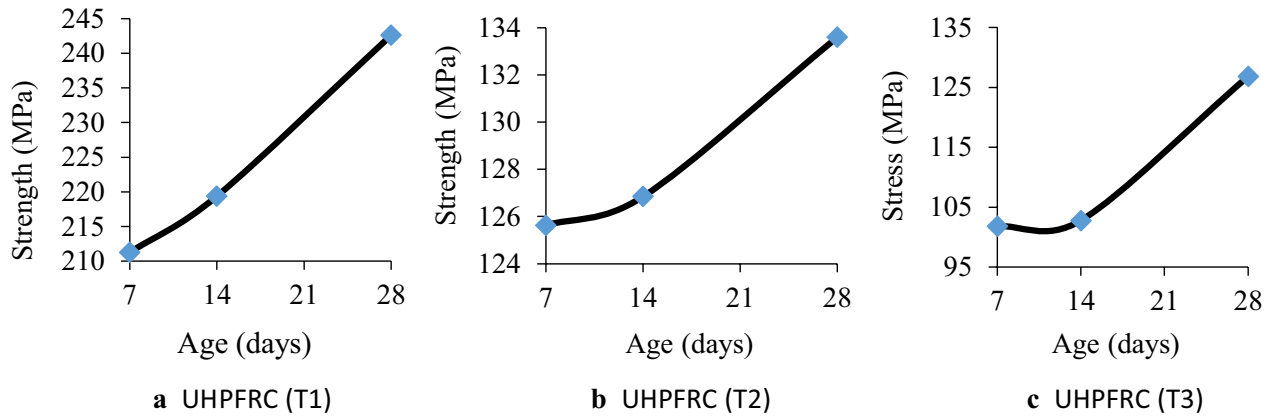

Fig. 11 Ultimate compressive strength gain with respect to age

The experimental outcomes showed that the concrete surface remained relatively in good shape despite failure (see Fig. 12). Figure 11b portrays the strength achieved at different specimen ages and the influence of fiber type on the optimum compressive strength. The compressive stress–strain curves for UHPFRC with Forta-Ferro synthetic fiber concrete (T3) at different ages are illustrated in Fig. 9c. It was observed that the elastic stage for T3 at different test periods indicated a similar trend up to the first crack. The elastic behavior of the UHPFRC specimens reached 55–60% of the compressive strength, and followed by strain hardening (compression) up to its ultimate strength. The fiber-matrix interaction contributed to ductile failure, as demonstrated by the concrete surface that was undamaged even at strength loss (see Fig. 13).

6.2 Uniaxial Tensile Test

The uniaxial tensile test was conducted on six specimens for each age (7, 14, and 28 days) and the average result was calculated for each mix design. The strain was obtained by dividing the average extension with the total length of the tampered section of the test sample, whereas the stress was achieved by dividing the machine load with the cross narrow section area of the specimens.

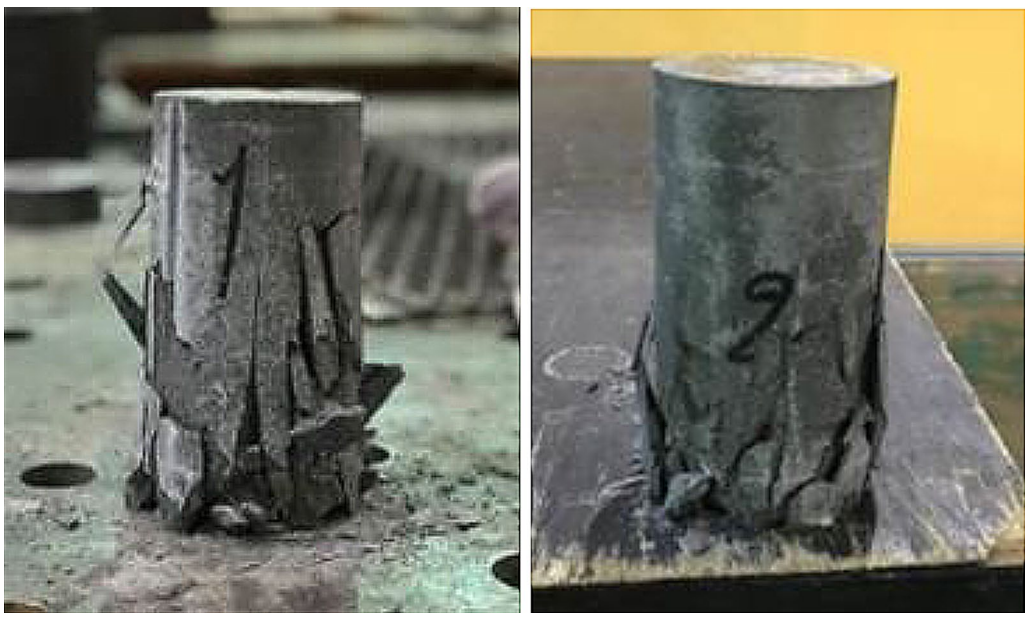

Fig. 12 Formation of cracks and UHPFRC with 5D steel fibers (T2) at failure of the compression tests

Fig. 13 Formation of cracks and UHPFRC (T3) steel fibers at failure of compression tests

Figure 14 portrays the tensile stress–strain curves at various ages (7, 14, and 28 days), which summarize the characteristic of material behavior for UHPFRC with micro and hooked ends steel fibers (T1), 5D steel fibers (T2), and Forta-Ferro synthetic fibers (T3).

6.2.1 Linear Elastic Phase

Specimen T1 displayed increment in elastic stage and material ductility. Next, specimen T2 showed increased elastic stage and better performance of the overall material behavior. Lastly, specimen T3 did not display any significant influence on the material behavior. The ultimate tensile strength achieved was the peak strength of the material. At this stage, the major part of the tensile strength was achieved with minimum or negligible deformation values.

6.2.2 Crack Developing Phase

The elastic phase was characterized by the formation and propagation of the initial cracks. The width of crack opening was determined by the fiber type, while the stress was conveyed by the bridging effect of the fibers across the transition zones or faces of each crack. Therefore, sufficient bond was needed between matrix and fibers to attain even distribution of fibers.

Specimen T1 controlled the crack opening width and the specimen was not fully damaged. The even distribution of this type of fiber gave sufficient bond between fiber and matrix. At the end of this stage, the deformation increased until the fibers pulled-out from the matrix (see Fig. 15a). The high length of 5D steel fibers, when compared to the dog-bone specimen dimensions, prevented the fibers to have an even distribution in the specimen, thus affecting the required bond between matrix and fibers (see Fig. 15b). The phase for 5D steel fibers was longer than the other types of fiber due to its high length and thickness that prevented it to fail to grip both sides of the micro cracks, thus sustaining the stress.

On the other hand, specimen T3 displayed good performance in reducing the crack opening width, while the stress was transferred through the bridging effect of the fibers across the transition zones at the beginning of this phase. As soon as the fibers failed to grip both sides of the micro cracks to sustain the stress, the deformation drastically increased and led to fiber tear that ended this phase (see Fig. 15c).

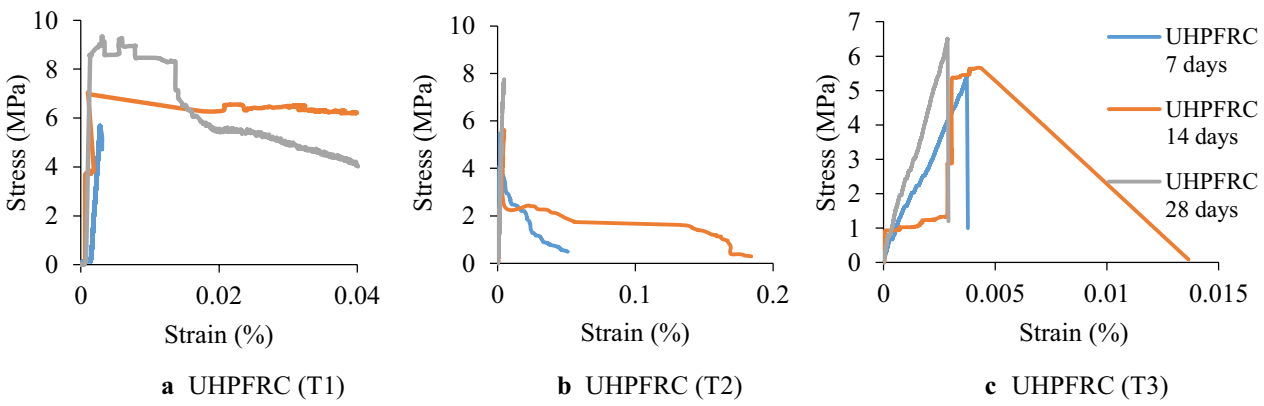

Fig. 14 Tensile Stress–Strain curve with respect to age

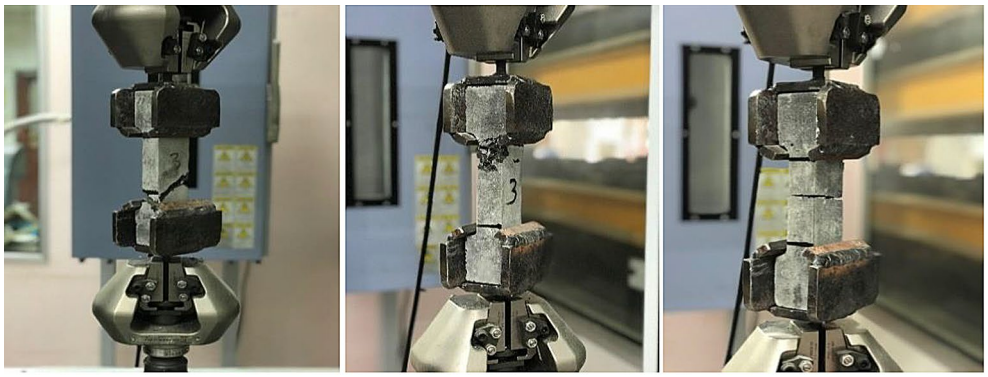

a UHPFRC (T1) b UHPFRC (T2) c UHPFRC (T3)

Fig. 15 Formation of macro crack and post peak failure of the uniaxial tensile

6.2.3 Failure phase

The failure stage of the UHPFRC began when the maximum tensile strength reached the strain hardening regime. Specimen localization was noted at its weakest point, which subsequently combined many micro cracks to develop a macro crack.

Thereafter, the stress–strain curve exceeded the elastic range; no longer signifying an average deformation, but localized distortion (Hillerborg 1985). The measurement recorded at this stage is referred to as crack mouth opening, while the strain was no longer uniformly distributed over the specimen length. Nonetheless, the volume, length, and shape properties of steel fibers in the matrix determined its ductility behavior.

Matrix strength and fiber length determined the pull-out behavior of the fiber in the specimen. Strain softening was observed to occur progressively in the presence of fiber, which was similar to its tensile behavior. It is difficult to predict softening curve shape for UHPFRC samples of different fiber types both in tension and compression. This is attributed to fiber orientation and distribution, which could be randomly or aligned in the concrete. In order to develop the constitutive model and propose the damage plasticity data of UHPFRC with different fiber types, the uniaxial tensile test outcomes of UHPFRC at 28 days were weighed in. For specimen T1, the crack opening width reached its maximum width, and the fibers started to slip from the matrix. The crack mouth opening was limited to the value related to half of the longest fiber length in the composite. Figure 16a displays the strength at different ages and the effect of fiber type on tensile strength. For specimen T2, the crack propagation was perpendicular to the direction of the specimen extension (see Fig. 15b). This led to slip between fibers and matrix, thus decreasing the stress pattern. The mouth of the crack opening was localized and this depended on the half length of the longest fiber. Figure 16b illustrates the maximum tensile strength

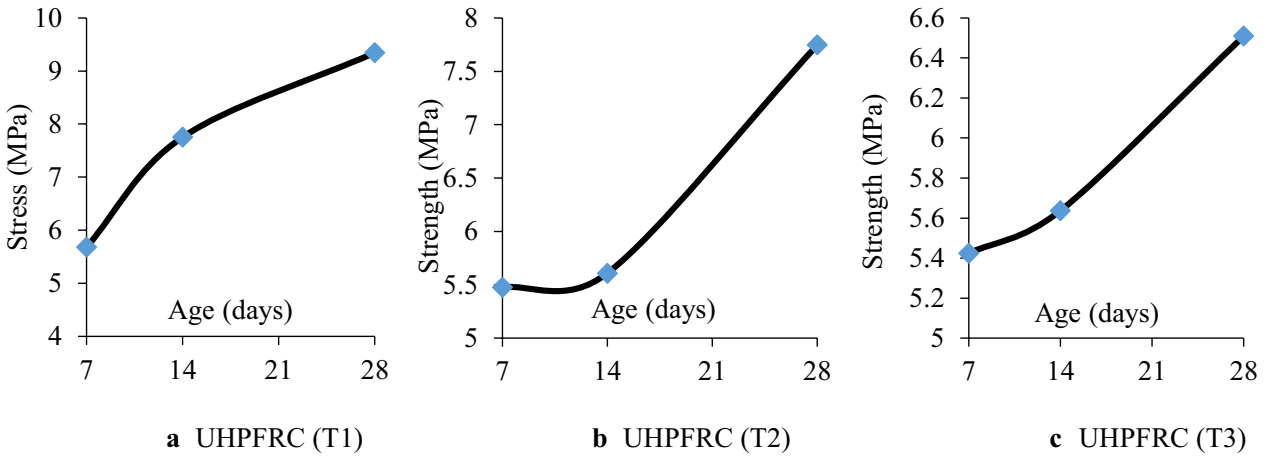

a UHPFRC (T1) **b** UHPFRC (T2) **c** UHPFRC (T3)

Fig. 16 Ultimate tensile strength gain with respect to age

at different ages. Only slight variance was noted for strength between T2 specimens tested on 7th and 28th day. The propagation of the crack was perpendicular to the direction of the specimen extension for specimen T3, which led to slip between the Forta-Ferro synthetic fibers and the matrix (see Fig. 15c).The difference in the prism section (76 or 126 mm) had no significant effect on the tensile strength of the concrete. Figure 16c displays the maximum tensile strength at different ages.

7 Developed Constitutive Model of UHPFRC with Different Types of Fiber

The constitutive model and the damage plasticity data served as the main parameters to develop the analytical model of materials to reflect the actual behavior of materials for structure simulations in numerical study. In this present study, the constitutive models for UHPFRC with different types of fiber were developed using outcomes retrieved from uniaxial compression and tension tests on the 28th day of aging. This is further described in the following sections:

7.1 UHPFRC with Micro and Hooked Ends Steel Fibers (T1)

Figure 17a presents the constitutive model for T1 developed based on the 28-day uniaxial compression test results. The maximum compressive stress was 242.61 MPa and the corresponding strain was 6897 $\mu\varepsilon$. As shown in Fig. 17a, a polynomial curve fitting up to the fourth degree as $y=-2E+11X^4+2E+09x^3-1E+06x^2+25601x$ with correlation factor of $R^2=0.98$ was determined as the best trend line to uniaxial compressive stress–strain curve.

The constitutive model and the damage plasticity data for T1 were obtained from the 28-day uniaxial tensile testing results, as depicted in Fig. 17b. The maximum tensile stress was 9.34 MPa, whereas the maximum strain was 3126 $\mu\varepsilon$. Figure 17b shows the polynomial curve fitting for the fifth degree equation as $y=2E+10x^5-1E+09x^4+4E+07x^3-66493x^2+4381.x$ with correlation factor of $R^2=0.887$, which was used for the stress–strain curve of the uniaxial tensile test. However, it failed to predict the softening part of the curve for T1 in tension and compression accurately. This is ascribed to random orientation and distribution of the micro and hooked ends steel fibers in the concrete.

Table 3 tabulates the testing results of ultimate compression, tensile stress vs strain, and Young's modulus of elasticity for specimens at the aforementioned test ages for T1.

The proposed constitutive model for T1 based on tension and compression is illustrated in Fig. 18a. Table 4

Table 3 Tensile and compressive stress–strain values with modulus of elasticity for UHPFRC (T1) at different ages

UHPFRC with micro and hooked ends steel fibers (T1)				
Age (days)	Maximum tensile stress (MPa)	Corresponding strain ($\mu\varepsilon$)	Maximum compressive stress (MPa)	Corresponding strain ($\mu\varepsilon$)
7	5.68	2775	211.27	2394
14	7.75	1028	219.38	5328
28	9.34	3126	242.61	6897

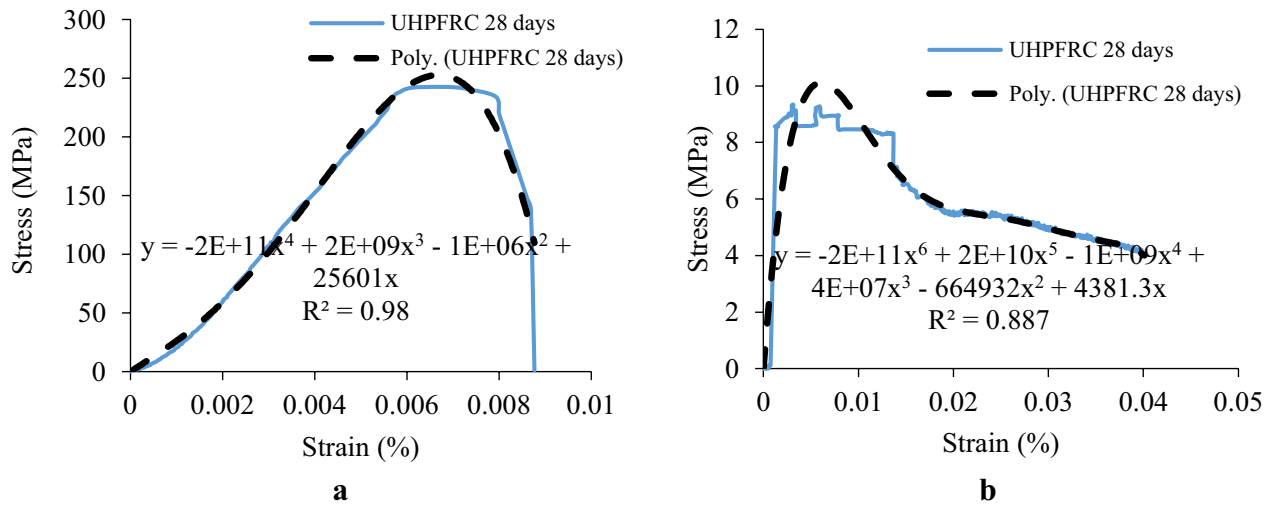

Fig. 17 Uniaxial **a** compressive and **b** tension stress–strain curve of UHPFRC (T1)

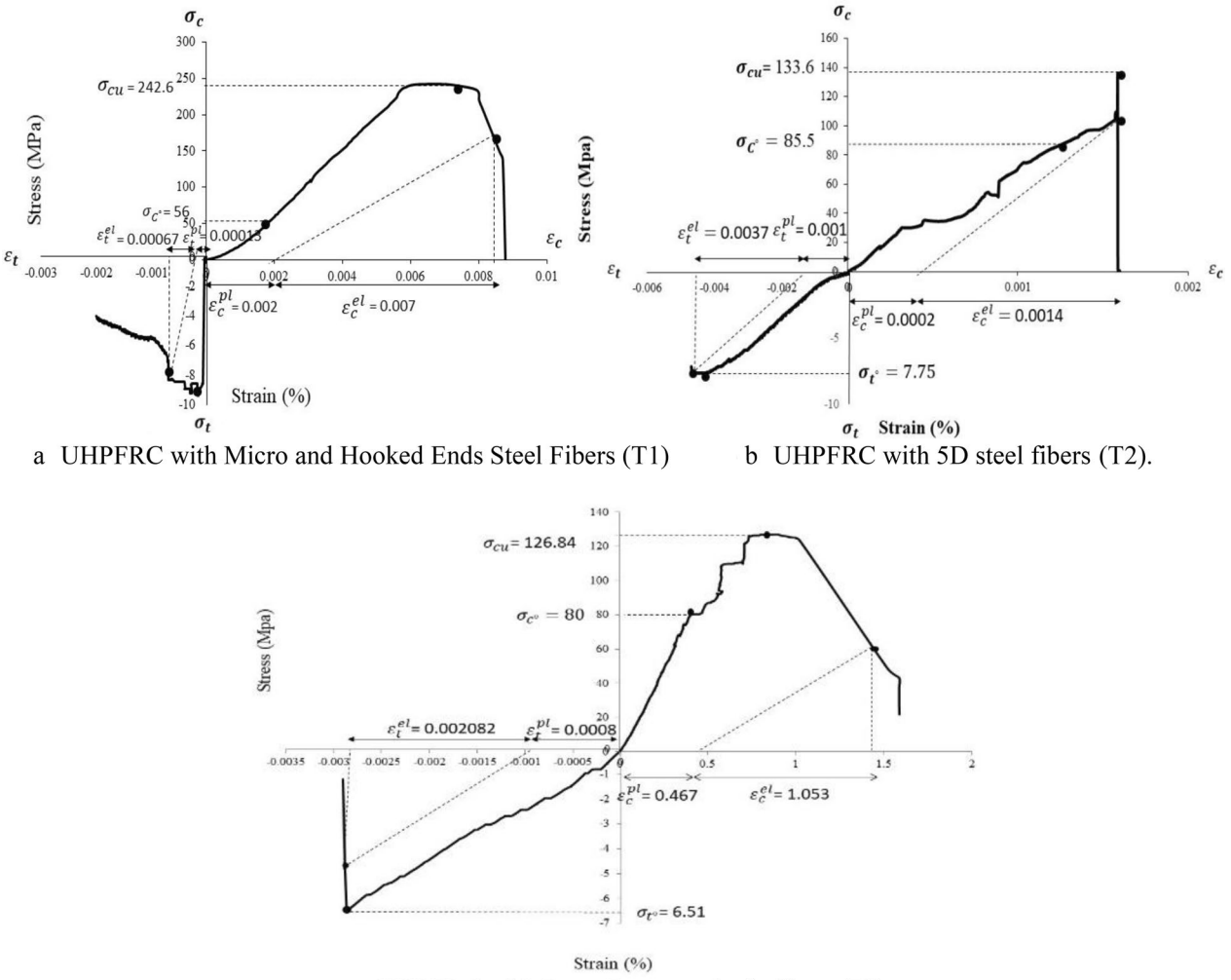

a UHPFRC with Micro and Hooked Ends Steel Fibers (T1)

b UHPFRC with 5D steel fibers (T2).

c UHPFRC with Forta-Ferro synthetic fibers (T3)

Fig. 18 Developed constitutive model for compressive and tensile behavior of the three different fiber types

lists the damage plasticity data derived from the aforementioned procedure for T1 in a tabular format.

7.2 UHPFRC with 5D Steel Fibers (T2)

In order to develop the compressive constitutive model and to propose the damage plasticity data for T2, the uniaxial compression test results at day 28 had been weighed in (see Fig. 19a). The maximum compressive stress for T2 was 133.6 MPa, which was achieved at the maximum strain of 1118 $\mu\varepsilon$. The sixth-order polynomial curve as $y = -3E{+}18x^6 + 4E{+}16x^5 - 1E{+}14x^4 + 2E{+}11x^3 - 2E{+}08x^2 + 110096x$ and correlation factor of $R^2 = 0.9929$ suited the uniaxial compressive stress–strain curve of T2.

Figure 19b illustrates the uniaxial tensile test results, which were employed to develop the constitutive model and to propose the damage plasticity data for T2. The maximum tensile stress of T2 and its corresponding strain were 7.75 MPa and 4665 $\mu\varepsilon$, respectively. A third-order polynomial curve with equation of $y = -1E{+}08x^3 + 940824x^2 + 395.54x$ and correlation factor of $R^2 = 0.9996$ had been adopted on the stress–strain curve achieved from the uniaxial tensile stress–strain curve of T2.

The ultimate compressive, the tensile stress vs strain values, and the Young's modulus of elasticity at different test ages for T2 are listed in Table 5.

The developed constitutive model of T2, as portrayed in Fig. 19, was implemented to simulate the cyclic behavior of circular flange bolted connections.

Table 6 shows the collected damage plasticity data of T2 presented in tabular format.

Table 4 Material properties for concrete with developed constitutive model in UHPFRC with micro and hooked ends (T1)

Material's parameters	UHPFRC (T1)	Plasticity parameters	
		Dilation angle	33
Concrete elasticity		Eccentricity	0.1
E (GPa)	30	*fb0*/*fc0*	1.16
N	0.2	(*K*)	0.67
		Viscosity parameter	0
Concrete compressive behavior		**Concrete compression damage**	
Yield stress (MPa)	**Inelastic strain**	**Damage parameter (C)**	**Inelastic strain**
0	0	0	0
29.04	0.001267	0	0.001267
47.9	0.001759	0	0.001759
80.8	0.002459	0	0.002459
150.2	0.003946	0	0.003946
198.9	0.005021	0	0.005021
226.9	0.005603	0	0.005603
242.6	0.006897	0	0.006897
220	0.008	0.09	0.008
192.7	0.008231	0.21	0.008231
183.6	0.008308	0.24	0.008308
174.5	0.008385	0.28	0.008385
156.3	0.008538	0.36	0.008538
147.2	0.008615	0.39	0.008615
138.1	0.008692	0.43	0.008692
1.1	0.008769	0.99	0.008769
Concrete tensile behavior		**Concrete tension damage**	
Yield stress (MPa)	**Cracking strain**	**Damage parameter (T)**	**Cracking strain**
9.34	0	0	0
0.000112	0.000156	0.99	0.000156

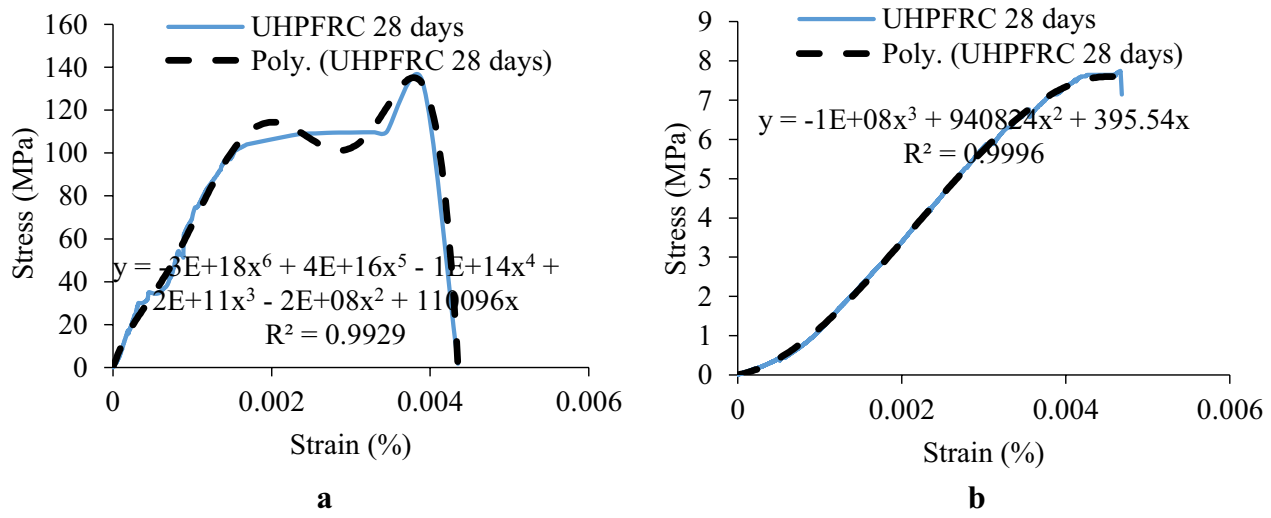

Fig. 19 Uniaxial **a** compressive and **b** tensile stress–strain curve of UHPFRC (T2)

Table 5 Tensile and compressive stress–strain values with modulus of elasticity for UHPFRC (T2) at different ages

Age (days)	UHPFRC with 5D steel fibers (T2)			
	Maximum tensile stress (MPa)	Corresponding strain ($\mu\varepsilon$)	Maximum compressive stress (MPa)	Corresponding strain ($\mu\varepsilon$)
7	5.48	1473	125.63	2623
14	5.61	4523	126.84	1118
28	7.75	4665	133.59	3900

7.3 UHPFRC with Forta-Ferro Synthetic Fibers (T3)

The uniaxial compression test results forT3 at day 28 were employed to develop the compressive constitutive model and to propose the damage plasticity parameters for T3 (see Fig. 20a).The maximum compressive stress was 126.84 MPa at the maximum strain of 2235 $\mu\varepsilon$. The polynomial curve fitting up to sixth degree was used to provide the best trend line based on the stress–strain curve as $y=4E{+}18x^6-4E{+}16x^5+1E{+}14x^4-2E{+}11x^3+2E{+}08x^2+33112x$ and correlation factor of $R^2=0.9948$.

Figure 20b illustrates the tensile constitutive model and the damage plasticity data for T3 obtained from the uniaxial tensile test results. The maximum tensile stress was 6.51 MPa, which was recorded at the corresponding strain of 2867 $\mu\varepsilon$. The third degree polynomial curve of $y=2E{+}08x^3-771862x^2+2997.8x$ with correlation factor of $R^2=0.9918$ fit the uniaxial tensile stress–strain curve of T3, as shown in Fig. 20b.

Table 7 presents the complete test outcomes for optimal compressive, tensile stress vs strain, and Young's modulus of elasticity at different test ages of the concrete samples.

The test results were consistent, thus justifying the simplicity and the validity of the developed methods. The developed constitutive model for T3, as portrayed in

Table 6 Material properties for concrete with developed constitutive model in UHPFRC with 5D steel fibers (T2)

Material's parameters	UHPFRC (T2)	Plasticity parameters	
		Dilation angle	33
Concrete elasticity		Eccentricity	0.1
E (GPa)	30	*fb*0/*fc*0	1.16
N	0.2	*K*	0.67
		Viscosity parameter	0
Concrete compressive behavior		**Concrete compression damage**	
Yield stress (MPa)	**Inelastic strain**	**Damage parameter C**	**Inelastic strain**
0	0	0	0
20.9	0.000242	0	0.000242
40.8	0.000708	0	0.000708
61.9	0.000893	0	0.000893
71.9	0.00101	0	0.00101
80.9	0.001147	0	0.001147
90.9	0.001328	0	0.001328
109.8	0.00345	0	0.00345
133.6	0.0039	0	0.0039
35.1	0.00435	0.73728	0.435
21.6	0.0046168	0.838421	0.0046168
16.2	0.0046255	0.878816	0.0046255
10.8	0.0046284	0.919211	0.0046284
5.4	0.0046371	0.959605	0.0046371
2.7	0.0046429	0.979803	0.0046429
Concrete tensile behavior		**Concrete tension damage**	
Yield stress (MPa)	**Cracking strain**	**Damage parameter T**	**Cracking strain**
7.75	0	0	0
0.00601	0.004665	0.999224	0.004665

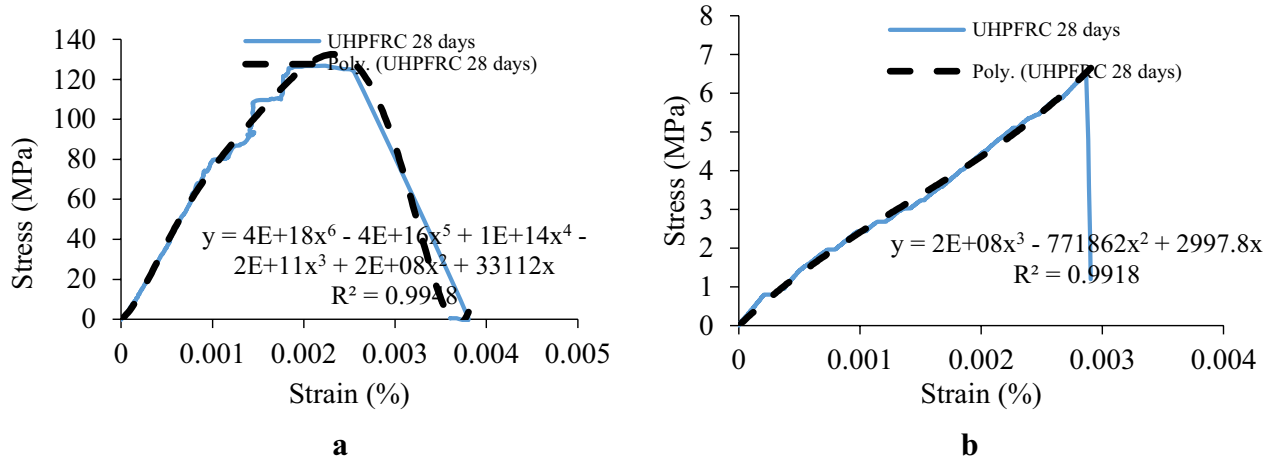

Fig. 20 Uniaxial **a** compressive and **b** tensile stress–strain curve of UHPFRC (T3)

Table 7 Tensile and compressive stress–strain values with modulus of elasticity for UHPFRC (T3) at different ages

UHPFRC with micro and hooked ends steel fibers (T3)				
Age (days)	**Maximum tensile stress (MPa)**	**Corresponding strain (*με*)**	**Maximum compressive stress (MPa)**	**Corresponding strain (*με*)**
7	5.42	3727	101.85	1662
14	5.64	4072	118.47	2735
28	6.509	2867	126.84	2235

Fig. 18c, was employed to simulate cyclic behavior of circular flange bolted connections. The parameters for damage plasticity, the variables of hardening and softening behavior, as well as the scalar damage data for compression and tension behavior for T3 are tabulated in Table 8.

8 Verification of the Developed Constitutive Models

The developed constitutive models and the damage plasticity data for the UHPFRCs were verified via numerical modelling of three hollow circular concrete columns reinforced with the three types of fiber. The numerical modeling was conducted by using the finite element method via ABAQUS commercial package. The results were compared with experimental findings based on the similar details of hollow columns retrieved from UHPFRC with different types of fiber.

The material properties (constitutive model and damage plasticity data) derived from uniaxial tensile and compressive laboratory tests were used in finite element model to validate the experimental findings.

The test was conducted by applying cyclic load using a dynamic actuator with 300 kN load capacity at the Structural Testing Laboratory, University Putra Malaysia. The column specimens were denoted as C1, C2, and C3 for T1, T2, and T3, respectively. The backbone curve corresponding to hysteresis loop results for experimental test and numerical analysis was plotted, as shown in Fig. 21, to compare the results of applied lateral loads versus displacement between experimental test and numerical analysis.

Figure 21 illustrates the results retrieved from the damage plasticity analysis, which was conducted by implementing the developed damage plasticity model for UHPFRCs with three different types of fiber, as well as images of the damages from the experimental test of hollow UHPFRC column subjected to cyclic load. Exceptional agreement was noted between the experimental testing results and the finite element analysis results for all the three mixed concrete materials. Nonetheless, as mentioned before, the slight difference in displacement results for C1 is attributed to sliding of column support during experimental testing, which led to 16% variation with numerical model.

This issue was addressed in the next testing procedure as the outcome showed 95% accuracy for displacement results.

The deformed shape and the crack propagation of the UHPFRC columns shown in Fig. 21 were predicted by conducting plasticity analysis of finite element model of hollow column, which had been developed using the derived concrete damage plasticity models for T1 (see Table 4), T2 (see Table 6), and T3 (see Table 8).

Figure 21 also illustrates the images of deformed shape and damaged UHPFRC columns after conducting the

Table 8 Material properties for concrete with developed constitutive model in UHPFRC with Forta-Ferro synthetic fibers (T3)

Material's parameters	UHPFRC (T2)	Plasticity parameters	
		Dilation angle	33
Concrete elasticity		Eccentricity	0.1
E (GPa)	30	*fb*0/*fc*0	1.16
ν	0.2	*K*	0.6
		Viscosity parameter	0
Concrete compressive behavior		**Concrete compression damage**	
Yield stress (MPa)	**inelastic strain**	**Damage parameter (C)**	**Inelastic strain**
20.9	0	0	0
39.9	0.000537	0	0.000537
47.7	0.000622	0	0.000622
55.8	0.000723	0	0.000723
68.1	0.000855	0	0.000855
89.7	0.001379	0	0.001379
102.8	0.001444	0	0.001444
110.9	0.00175	0	0.00175
126.8	0.002235	0	0.002235
126.3	0.002288	0.004	0.002288
125.1	0.00244	0.014	0.00244
123.5	0.002553	0.027	0.002553
48.6	0.003802	0.62	0.003802
43.2	0.003674	0.66	0.003674
37.8	0.003622	0.70	0.003622
5.4	0.003607	0.96	0.003607
Concrete tensile behavior		**Concrete tension damage**	
Yield stress (MPa)	**Cracking strain**	**Damage parameter (T)**	**Cracking strain**
6.5	0	0	0
0.0014	0.002867	0.999778	0.002867

experimental test by applying cyclic load using a dynamic actuator with 300 kN load capacity. By comparing the location of damages, cracks, and deformed shape of the columns resulted from numerical simulations with experimental testing results, it was observed that the finite element plasticity analysis that used the developed Concrete Damage Plasticity model in this study had managed to predict load–displacement curves and crack propagation with good agreement and reasonable accuracy. Based onthe presented results and discussion, it is confirmed that the developed constitutive models and the concrete damage plasticity data can be implemented to numerically simulate UHPFRC materials with micro and hooked ends steel fibers, Bekaert Dramix 5D steel fibers, and Forta-Ferro synthetic fibers under static and dynamic loadings. The energy dissipation capacity of the column specimen subjected to cyclic loading was calculated as the area under the load–displacement curves, as presented in Table 9. Based on the experimental testing results, the energy dissipation as area of under load–deflection curve had been 2.83 kN m, 2.75 kN m, and 2.61 kN m for hollow columns C1, C2, and C3, respectively. From the finite element analysis results, the energy dissipation capacities were 3.024 kN m, 3.0 kN m, and 2.93 for hollow columns C1, C2, and C3, respectively. The results signified that C1 exhibited slightly more energy dissipation, when compared to C2 and C3. The polynomial curves were adopted for the force–displacement responses deriving from experimental test and finite element analysis results for hollow columns C1, C2 (see Fig. 21b), and C3 (Fig. 21c), in order to provide the best line trend (see Fig. 21). Upon comparing the results of experimental tests between the three columns, it was found that the lateral load capacity for C2 was 15% higher than that of C3. The maximum load capacity for C1 was 6.5% higher than C2. However, all UHPFRC

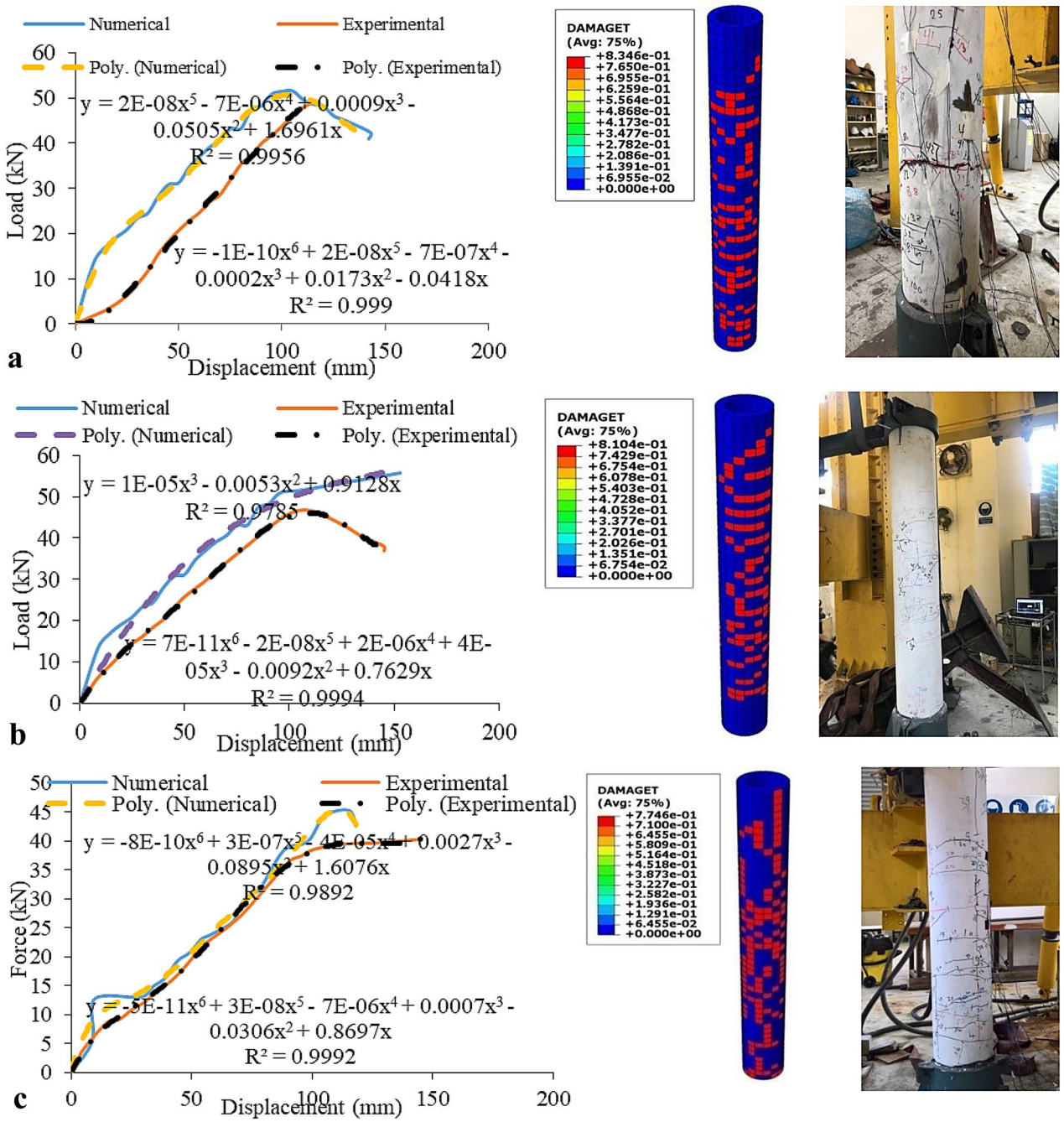

Fig. 21 Load-deflection curves obtained from the numerical model and test results at top of the columns **a** C1, **b** C2 and **c** C3

columns exhibited almost similar ductility and deformation capacity.

9 Conclusion

This study had looked into the development of constitutive models and the evaluation of damage plasticity data for UHPFRC with micro and hooked ends steel fibers (T1), Bekaert Dramix 5D steel fibers (T2), and Forta-Ferro synthetic fibers (T3).

The uniaxial compression and tensile tests for cylinder and dog-bone specimens casted using the selected types of fiber had been conducted. The hollow thin circular columns with different types of fiber were empirically tested by subjecting to cyclic load to verify the finite element

Table 9 Comparison of numerical and test results at top of the columns (C1, 2 and 3)

Specimen	Test	Displacement (mm)	Percentage difference (%)	Ultimate load (kN)	Percentage difference (%)	Energy dissipation (kN m)	Percentage difference (%)
C1	Numerical	143	–	51.51	–	3.024	–
	Experimental	120.13	16	49.12	4.6	2.83	6.8
C2	Numerical	153.06	–	55.73	–	3	–
	Experimental	145.2	5.14	46.51	16.5	2.75	9.0
C3	Numerical	142	–	45.32	–	2.93	–
	Experimental	145.2	2.2	40.4	12.5	2.61	10

simulation developed using the proposed new concretes analytical model.

As a result, it was found that adding micro and hooked ends steel fibers in the UHPFRC did improve the performance of the concrete by 45% and 47.7%, respectively, besides increasing the compressive strength of the concrete by 45% at day 28. The semicro and hooked-end steel fibers led to more energy consumption after yielding concrete section upon load application. Next, the use of 5D fibers increased the compressive strength by 5%, when compared to that of Forta-Ferro synthetic fibers. The experimental test for C1 under cyclic loads revealed 6.5% and 22.5% higher maximum load capacities, in comparison to C2 and C3, respectively. However, all UHPFRC columns displayed almost similar ductility and deformation capacity. No serious spalling of the concrete cover was noted for all three hollow column segments due to the high bond stress between concrete and fibers.

Both the experimental and FEM results showed that the three fiber types had efficiently increased both initial and ultimate load capacities. Besides, no shear failure occurred for all the specimens due to high shear capacity of UHPFRC for all three fiber types. The results of FEA analysis, which were implemented to the developed constitutive and damage plasticity models, were in agreement with the experimental outcomes with less than 10% discrepancies for lateral resistance. Hence, the proposed constitutive model and the derived concrete damage plasticity parameters are indeed applicable for any numerical simulation and finite element modeling of structural concrete with micro and hooked ends steel fibers, Bekaert Dramix 5D steel fibers, and Forta-Ferro synthetic fibers.

Acknowledgements
This research work receives support from DURA TECHNOLOGY SDN. BHD. company under a research grant provided by Ministry of Science Technology & Innovation, Malaysia, entitled "Development and construction of Internet Transmission Tower Using Ultra High Performance Concrete". Also, this research is supported by FORTA CORPORATION and INNOFLOOR SDN BHD companies and received further support from BEKAERT and BEKAERT SHAH ALAM SDN BHD company.

Their help and support are gratefully acknowledged.

Authors' contribution
DTH: Developed numerical model and performed FEM simulation. Conducted the experimental test. FH: Lead the research project. Developed the concept of constitutive model and damage plasticity. Elaborated and interpret the results. VYL: Proposed the UHPFRC material properties and casting specimens. All authors read and approved the final manuscript.

Authors' information
Doaa Talib Hashim received the B.Sc. degree in Civil Engineering from College of Engineering, Mustansiriyah University, Baghdad (Iraq) on 2011. She continued her master study in Structural and Construction Engineering and her PhD in Structural Engineering in University Putra Malaysia and completed her study in 2015 and 2019, respectively. She is currently a lecturer at Mustansiriyah University, Baghdad (Iraq). Her areas of interest include earthquake engineering, mechanics of material, structural dynamic, solid mechanics and finite elements.

Farzad Hejazi is Associate Professor and Research Coordinator at Department of Civil Engineering, Faculty of Engineering, University Putra Malaysia (UPM). Also currently he is Senior Visiting Academic in University of Sheffield. His specific field of expertise are Structural Engineering, Structural Dynamic, Reinforced concrete Structures, Vibration, Finite Element Method, Inelastic Analysis, Earthquake, Damper Device, Vibration Dissipation Systems, Active and Passive Structural Control Systems, Optimization, Computer Program Coding, Structure Simulation.

Voo Yen Lei is the founder of Dura Technology, which specialises in the manufacturing of precast concrete products made from Ultra-High-Performance Concrete. To-date Dura Company has supplied 130 over UHPC bridges in Malaysia, and has also transferred the technology to China, India and Canada. He also an Adjunct Professor with the University of New South Wales, Australia. He was awarded the 2016 PCI Design Award Winner: Best International Transportation Structure on Construction of the 100m Single Span Batu 6 UHPFRC Bridge from the USA Precast/Prestressed Concrete Institution.

Competing interests
The authors declare that they have no conflict of interest.

Author details
[1] Department of Civil Engineering Faculty, University Putra Malaysia, Serdang, Selangor 43400, Malaysia. [2] Dura Technology Sdn Bhd, Ipoh, Malaysia.

Received: 30 June 2019 Accepted: 16 May 2020
Published online: 31 July 2020

References

ASTM. (2002). *Standard Test Method for Static Modulus of Elasticity and Poisson's Ratio of Concrete in Compression; Annual Book of ASTM Standards* (p. 469). West Conshohocken: ASTM.

Aydın, S., & Baradan, B. (2013). The effect of fiber properties on high performance alkali-activated slag/silica fume mortars. *Compos Part B-Eng, 45*(1), 63–69.

Bofang, Z. (2013). Thermal stresses and temperature control of mass concrete. Butterworth-Heinemann.
El-Dieb, A. S. (2009). Mechanical, durability and microstructural characteristics of ultra-high-strength self-compacting concrete incorporating steel fibers. *Mater Design, 30*(10), 4286–4292.
Farzad, M., Fancy, S. F., Azizinamini, A., Lau, K. (2019, May). Effect of concrete moisture on Macrocell development in repair of reinforced concrete substructure with UHPC. In: *Corrosion 2019*. NACE International.
Ferrara, L., Ozyurt, N., & Di Prisco, M. (2011). High mechanical performance of fibre reinforced cementitious composites: The role of "casting-flow induced" fibre orientation. *Materials and Structures, 44*(1), 109–128.
Grassl, P., Xenos, D., Nyström, U., Rempling, R., & Gylltoft, K. (2013). CDPM2: A damage-plasticity approach to modelling the failure of concrete. *International Journal of Solids and Structures, 50*(24), 3805–3816.
Graybeal, B. A. (2006). Material property characterization of ultra-high performance concrete (No. FHWA-HRT-06-103).
Hassan, A. M. T., Jones, S. W., & Mahmud, G. H. (2012). Experimental test methods to determine the uniaxial tensile and compressive behaviour of ultra high performance fibre reinforced concrete (UHPFRC). *Construction and Building Materials, 37,* 874–882.
Hillerborg, A. (1985). The theoretical basis of a method to determine the fracture energy G F of concrete. *Materials and Structures, 18*(4), 291–296.
Hognestad, E. (1951). *Study of combined bending and axial load in reinforced concrete members. Engineering Experiment Station*. Illinois: University of Illinois at Urbana Champaign, College of Engineering.
Kent, D.C., Park, R. (1971). Flexural members with confined concrete. J struct div.
Kim, D., Naaman, A. E., El-Tawil, S. (2008). High tensile strength strain-hardening FRC composites with less than 2% fiber content. In: Proceedings of second international symposium on ultra high performance concrete, Kassel, Germany (pp. 169–176).
Lankard DR (1972) Prediction of the flexural strength properties of steel fibrous concrete. In: Proceedings, CERL Conference on Fibrous Concrete, Construction Engineering Research Laboratory, Champaign (pp. 101–123).
Li, V. C. (2012). Tailoring ECC for special attributes: A review. *Int J Concr Struct M, 6*(3), 135–144.
Lu, X., & Hsu, C. T. T. (2006). Behavior of high strength concrete with and without steel fiber reinforcement in triaxial compression. *Cement Concrete Research, 36*(9), 1679–1685.
Mahmud, G. H., Yang, Z., & Hassan, A. M. (2013). Experimental and numerical studies of size effects of ultra high performance steel fibre reinforced concrete (UHPFRC) beams. *Construction and Building Materials, 48,* 1027–1034.
Naaman, A. E., Wille, K. (2012). The path to ultra-high performance fiber reinforced concrete (UHP-FRC): five decades of progress. In: Proceedings of Hipermat, 3–15.
Ng TS, Htut TNS, Foster SJ (2016) Steel fibre reinforced concrete: From X-ray imaging observation to modelling. In: The second international conference on science, engineering and environment (pp. 407–414).
Richard, P., & Cheyrezy, M. (1995). Composition of reactive powder concretes. *Cement and Concrete Research, 25*(7), 1501–1511.
Rossi, P. (2008). Ultra high performance concretes. *Concrete International, 30*(02), 31–34.
Rossi, P. (2013). Influence of fibre geometry and matrix maturity on the mechanical performance of ultra high-performance cement-based composites. *Cement Concrete Comp, 37,* 246–248.
Rossi, P., Arca, A., Parant, E., & Fakhri, P. (2005). Bending and compressive behaviours of a new cement composite. *Cement and Concrete Research, 35*(1), 27–33.
Wille, K., El-Tawil, S., & Naaman, A. E. (2014). Properties of strain hardening ultra high performance fiber reinforced concrete (UHP-FRC) under direct tensile loading. *Cement Concrete Compound, 48,* 53–66.
Wuest, J., EPF C. E., Brühwiler, E., ETH, D. C. E. (2008). Model for predicting the UHPFRC tensile hardening. In: Ultra High Performance Concrete (UHPC): Proceedings of the Second International Symposium on Ultra High Performance Concrete, Kassel, Germany, March 05-07, 2008 (No. 10, p. 153). Kassel University press GmbH.
Yang, S. L., Millard, S. G., Soutsos, M. N., Barnett, S. J., & Le, T. T. (2009). Influence of aggregate and curing regime on the mechanical properties of ultra-high performance fibre reinforced concrete (UHPFRC). *Construction and Building Materials, 23*(6), 2291–2298.
Yoo, D. Y., Kang, S. T., Lee, J. H., & Yoon, Y. S. (2013a). Effect of shrinkage reducing admixture on tensile and flexural behaviors of UHPFRC considering fiber distribution characteristics. *Cement and Concrete Research, 54,* 180–190.
Yoo, D. Y., Lee, J. H., & Yoon, Y. S. (2013b). Effect of fiber content on mechanical and fracture properties of ultra high performance fiber reinforced cementitious composites. *Composite Structures, 106,* 742–753.
Yu, R., Spiesz, P., & Brouwers, H. J. H. (2015). Development of ultra-high performance fibre reinforced concrete (UHPFRC): Towards an efficient utilization of binders and fibres. *Construction and Building Materials, 79,* 273–282.
Yunsheng, Z., Wei, S., Sifeng, L., Chujie, J., & Jianzhong, L. (2008). Preparation of C200 green reactive powder concrete and its static–dynamic behaviors. *Cement Concrete Comp, 30*(9), 831–838.

Publisher's Note